Inorganic Chemistry

Article

pubs.acs.org/IC

A Homoleptic Trisbidentate Ru(II) Complex of a Novel Bidentate Biheteroaromatic Ligand Based on Quinoline and Pyrazole Groups: Structural, Electrochemical, Photophysical, and Computational Characterization

Martin Jarenmark,[†] Lisa A. Fredin,[‡] Joachim H. J. Hedberg,[§] Isa Doverbratt,[†] Petter Persson,[‡] and Maria Abrahamsson*[,§]

[†]Centre for Analysis and Synthesis, Department of Chemistry and [‡]Theoretical Chemistry Division, Chemical Center, Lund University, Box 124, SE-22100 Lund, Sweden

[§]Department of Chemical and Biological Engineering, Chalmers University of Technology, SE-41296 Gothenburg, Sweden

Supporting Information

ABSTRACT: We synthesized a new homoleptic, tris-bidentate complex $[Ru(QPzH)_3]^{2+}$ based on the novel biheteroaromatic, 8-(3-pyrazolyl)-quinoline ligand QPzH. The QPzH ligand was designed to reduce the distortions typically observed in complexes incorporating the 8-quinolinyl group into the ligand framework. This was indeed observed, and was also, as anticipated, found to facilitate the formation of tris-homoleptic Ru(II) complexes; $[Ru(QPzH)_3]^{2+}$ is the first reported tris-homoleptic complex with ligands based on the 8-quinolinyl group. The synthesis can either result in a statistical 3:1 *mer*/*fac* ratio of the complex, or, through controlled exposure to light, be tweaked to allow isolation of the pure *mer* isomer only. X-ray crystallography reveals three nonequivalent ligands, with significantly less strain than other quinoline-based bidentate ligands. The complex exhibits a nearly octahedral coordination geometry but shows large differences in bond lengths between the Ru core and the quinoline and pyrazoles, respectively. The Ru−N(pyrazole) bond distances are ∼2.04 Å, while the corresponding distances for Ru−N(quinoline) are ∼2.12 Å. Structural, photophysical, electrochemical, and theoretical characterization revealed a *mer*-Ru(II) complex with a low oxidation potential (0.57 V vs ferrocene$^{0/+}$) attributed to the incorporation of the pyrazolyl group, a ground state absorption that is sensitive to the local environment of the complex, and a short-lived ^{3}MLCT excited state.

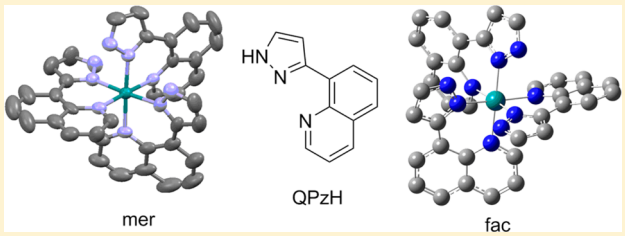

INTRODUCTION

Ruthenium polypyridyl complexes like the tris-bidentate $[Ru(bpy)_3]^{2+}$ (bpy is 2,2′-bipyridine) and bis-tridentate $[Ru(tpy)_2]^{2+}$ (tpy is 2,2′:6′,2″-terpyridine) have attracted much attention over many decades due to their favorable excited-state properties. They have proved useful for photosensitization purposes, as sensors and local environment probes and in molecular electronics applications.[1−7] Their electrochemical and photophysical properties are highly sensitive to the ligand structure and can be tuned by addition of substituents on the parent polypyridyl framework.[8] Commonly, the 4 and 4′ positions of the ligand framework are the target of substitution.[8,9] Substitutions in the 3,3′ positions are rare due to steric hindrance and the change in geometry that follows.[10] Reports of 5,5′ substitution exist, but are few in comparison, and also seem to result in less favorable photophysical properties.[11] Typically, for substitution in the 4 and 4′ positions, the effects on redox properties and on absorption and emission spectra can be predicted from the nature of the substituents, for example, electron-donating or -withdrawing groups.[8,12,13]

However, while modifying substituents on the parent bipyridine or the tridentate terpyridine frameworks mainly results in changes of the electronic properties of the complexes, incorporation of different heterocycles in biheteroaromatic ligands influences both the electronic properties and the coordination geometry of the complexes.[14] Indeed, ligand field theory suggests that the coordination geometry will have a large impact on the relative energies of the metal-to-ligand charge transfer (^{3}MLCT) state and the metal centered state (^{3}MC) in the excited-state manifold, which opens up another pathway for further tuning of properties of such complexes.[3,8,15,16] One example is the excited-state lifetime, where it has been shown that bis-tridentate Ru(II) complexes can experience a significant increase when the coordination sphere is modified to become more octahedral.[17−20] One of the most striking examples is the introduction of two 8-quinolinyl groups with a pyridine ring to form the tridentate ligand 2,6-bis(8-quinolinyl)-pyridine (DQP) with expanded, six-membered chelate rings. This

Received: July 11, 2014
Published: November 24, 2014

   dx.doi.org/10.1021/ic502432c | *Inorg. Chem.* 2014, 53, 12778−12790

yielded homoleptic Ru(II) complexes, with a nearly perfect octahedral coordination and microseconds excited-state lifetimes,[18,19] ~4 orders of magnitude longer than the 0.25 ns observed for $[Ru(tpy)_2]^{2+}$.[3] Further modifications of the DQP complex, both by core modifications and substituents, have since been reported.[21−23]

The encouraging results for $[Ru(DQP)_2]^{2+}$ and derivatives are in sharp contrast to the observation that the tris-bidentate complex $[Ru(bpy)_2(QPy)]^{2+}$, where QPy is 8-(pyridin-2′-yl)quinoline and a bidentate analogue to DQP, is virtually nonemissive at room temperature.[17] This intriguing fact deserves further investigation; however, a straightforward structural comparison between tridentate and bidentate complexes is hampered by the fact that, to the best of our knowledge, only heteroleptic Ru(II) complexes of bidentate biheteroaromatic ligands based on the 8-quinolinyl group have been reported. The reason for this may be found in the reports[24,25] of significant distortions and strain upon coordination of 8-quinolinyl-pyridine ligands to form metal complexes, something that can significantly influence the stability of the complexes.[17,26]

One way to facilitate the formation of homoleptic tris-bidentate Ru complexes of 8-quinolinyl ligands and simultaneously execute control over redox and photophysical properties is to combine the quinoline motif with a five-membered heterocycle, thus reducing some of the strain and structural distortions that have been observed in both $[Ru(DQP)_2]^{2+}$ and $[Ru(bpy)_2(QPy)]^{2+}$.[17−19] Introduction of a five-membered heterocycle instead of the pyridyl group would first decrease the bite angle of the ligand (Scheme 1) and thus allow for better accommodation of the longer metal−nitrogen bonds within the metallacycle. Second, the hydrogens on the backside of the ligand will be further displaced from each other, which should decrease their steric interaction, and hence they can be pushed toward each other to a greater extent, compared to a case with a pyridyl group bound in position 8 of the quinoline. The five-membered heterocycle used in this study, the pyrazolyl (PzH), is in itself a noninnocent ligand that is known to, for example, show significant sensitivity to the local environment such that the −NH group can interact strongly with the solvent or other complexes to form hydrogen bonds or be deprotonated, something that will also affect electrochemical and photophysical properties.[27−29] This makes for an interesting homoleptic Ru(II) complex, utilizing the novel QPzH ligand, where the photophysical and electrochemical properties depend simultaneously on the central metal coordination and outer sphere interactions. The homoleptic nature of the complex also allows for more extensive and straightforward comparisons with tridentate complexes like $[Ru(DQP)_2]^{2+}$.

In this study, we combine two ligand motifs with quite different properties; the 8-quinolinyl group accompanied by a five-membered heterocyclic pyrazole group, see Scheme 1, to form the QPzH ligand and the $[Ru(QPzH)_3]^{2+}$ complex. Structural, photophysical, and electrochemical properties of $[Ru(QPzH)_3]^{2+}$ are compared with quantum chemical calculations, which provide significant insights into the fundamental structural and electronic properties of metal complexes.[30,31] These calculations have, among other things, provided identification of ^{3}MLCT and ^{3}MC stationary points.[32,33] The progress in computational modeling of excited-state properties in recent years includes extensive use of time-dependent (TD) density functional theory (DFT) calculations to study optical absorption spectra of many light-harvesting complexes with good accuracy.[34] Experimental and computed data for $[Ru(QPzH)_3]^{2+}$ reveal that the combination of quinolinyl and pyrazolyl groups into the ligand results in a ligand that can adopt different conformations once it is coordinated to ruthenium, such that the internal strain of the ligand is reduced, but at the expense of increased steric interactions around the metal, manifesting in large differences in bond distances to the metal.

Scheme 1. Three Q-ligands Discussed in This Paper (QPzH, QPy, and DQP), and a Schematic Illustration of the Geometrical Differences between Bidentate Quinoline Ligands Incorporating five- (red) or six- (black) membered heterocycles[a]

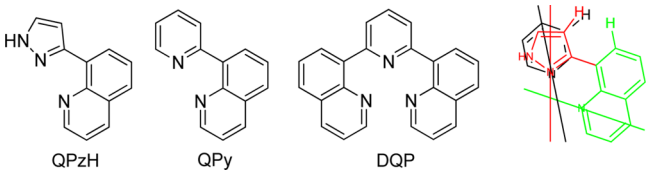

[a]The quinoline groups (green) are perfectly overlaid, and trend lines are added to show the directionality of the coordinating nitrogen lone pairs. The angle between the green and red or black lines indicate the inherent bite angle of the ligand.

RESULTS

Synthesis and NMR Characterization. The ligand 8-(3-pyrazolyl)-quinoline (**3** or QPzH in Scheme 2) was synthesized in two steps from 8-acetyl-quinoline (**1**), which was readily available from literature procedures.[35] The intermediate 3-(dimethylamino)-1-(8-quinoline)prop-2-en-1-one (**2**) could be

Scheme 2. Synthesis of the Ligand 3 (QPzH) and Complex $[Ru(QPzH)_3](PF_6)_2$[a]

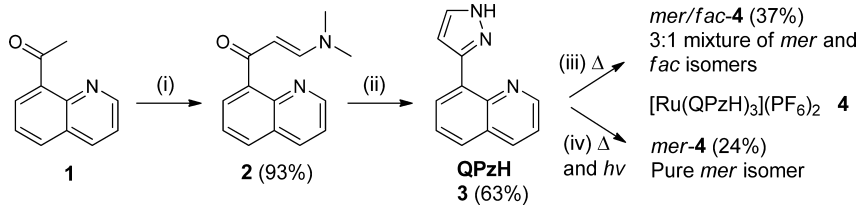

[a]Reactants, reagents, and conditions used: (i) dimethylformamide dimethylacetal (DMF-DMA), L-proline, 80 °C. (ii) Hydrazine monohydrate, ethanol, reflux. (iii) 1/3$Ru(DMSO)_4Cl_2$, ethylene glycol, 195°C 4 min, dark, followed by $NaPF_6$(aq) and HPF_6(aq). (iv) Same procedure as in (iii) but before precipitation of the product the reaction mixture was diluted and irradiated with visible light for 6 h.

dx.doi.org/10.1021/ic502432c | Inorg. Chem. 2014, 53, 12778−12790

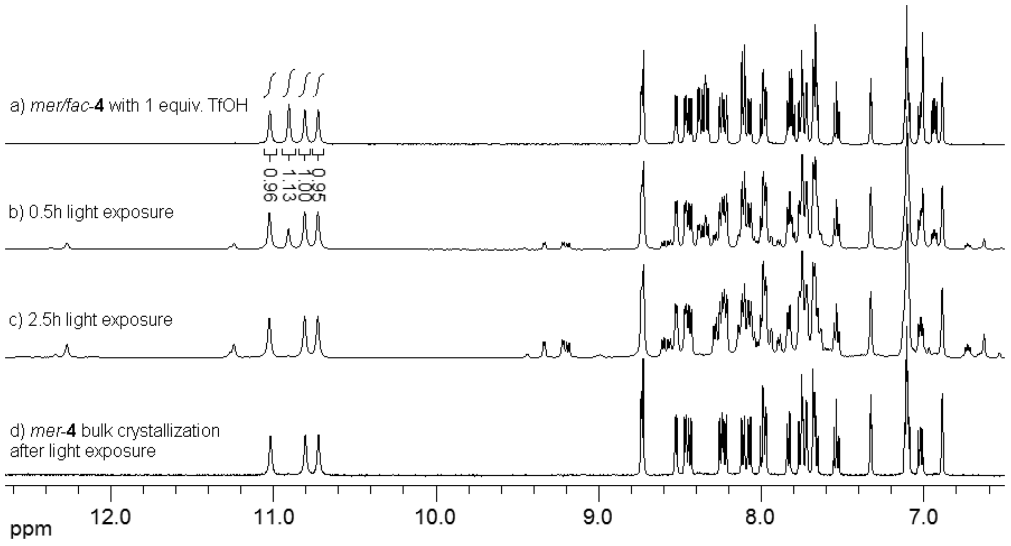

Figure 1. ^{1}H NMR spectra of *mer*/*fac*-**4** CD_3CN with 1 equiv of triflic acid displaying the integral values for the N−H pyrazole protons (a). This same sample was then exposed to light for 0.5 h (b) and 2.5 h (c). In (d) the ^{1}H NMR spectrum of the crystalline product, isolated after light exposure of the crude *mer*/*fac* mixture in a bulk synthesis of *mer*-**4**, is displayed, and it was also collected in CD_3CN with 1 equiv of triflic acid.

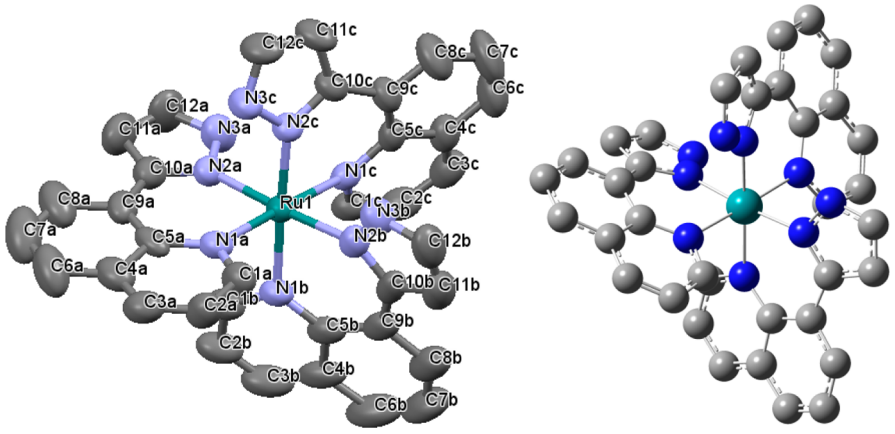

Figure 2. (left) Crystal structure of *mer*-**4** determined by single-crystal X-ray diffraction, plotted using Mercury.[42] Ellipsoids are drawn at 50% probability. (right) The optimized GS geometry of the *mer* isomer of $[Ru(QPzH)_3]^{2+}$. (The *fac* isomer is available in Supporting Information, Figure S4).

produced in excellent yield by an L-proline catalyzed condensation of dimethylformamide dimethylacetal (DMF-DMA) and (**1**). The following condensation of hydrazine with **2** yielded the ligand in reasonable yield. The complex $[Ru(QPzH)_3](PF_6)_2$ (**4**) was then assembled by heating the ligand together with $[Ru(DMSO)_4Cl_2]$ (DMSO = dimethyl sulfoxide) at high temperature for a short time. The high temperature made the complex form readily within a few minutes, which was beneficial since prolonged heating generally resulted in more side products regardless of temperature. Through this thermal process a statistical mixture (3:1) of *mer* and *fac* isomers formed, as observed by ^{1}H NMR (Figure 1a), but the two isomers could not be separated. The ^{1}H NMR could be integrated to match 36 independent proton resonances, and while the spectrum was crowded, many of the signals resolved well, making the estimation of the ratio between the isomers easy. The peaks from the protons on the nitrogen atoms of the pyrazole rings (N3 in Figure 2, *vide infra*) were typically broad and unresolved. Addition of triflic acid (TfOH) makes these peaks sharper and completely resolved into four resonances in the same region and with the same integration values. The NMR data for the complexes is reported for spectra collected in the presence of 1 equiv of TfOH to ensure complete protonation (Figure 1a). The fact that four resonances from the pyrazole N−H protons, with equal size of their integrals were observed, correlates well with what is expected for a mixture of *mer* and *fac* isomers in a 3:1 ratio since the N3 protons in the *fac* isomer are all equivalent, while in the *mer* isomer they all experience different environments.[36] The complete ^{1}H NMR spectrum of the complex, with and without acid, can be found in the Supporting Information (Figure S1).

The exact ratio between the isomers was poorly reproducible until it was discovered that leaving the reaction mixture in normal room light for several hours increased the ratio of *mer* to *fac*. The *mer* isomer could then be produced in the pure form by illumination of the *mer*/*fac* mixture using an external visible light source (see Experimental Section for details). No heating was required for this process. Furthermore, the reproducibility of the 3:1 ratio was increased if the exposure to light was minimized during synthesis. Since the *mer* isomer could be isolated in a pure form the resonances for the *fac* isomer could

dx.doi.org/10.1021/ic502432c | *Inorg. Chem.* 2014, 53, 12778−12790

largely be assigned in the sample containing the mixture of isomers. Isolation of the pure *fac* isomer has not been possible.

To investigate the selective decomposition of the *fac* isomer, a solution of the *mer*/*fac* mixture of **4** dissolved in CD_3CN, with 1 equiv of TfOH added, was exposed to light, and changes were monitored by ^1H NMR at regular intervals (Figure 1b,c, the full spectra are available in Supporting Information, Figure S1). While all resonances for the *fac* isomer are affected, the changes are most clearly observed for the N−H resonances of the pyrazoles. The rate of *fac* isomer N−H resonance disappearance is similar to the rate with which new resonances appear downfield. No significant changes are observed for the *mer* isomer, although minor decomposition cannot be excluded. The identity of the species formed is unknown; however, several of the new peaks are reminiscent of peaks for protonated, noncomplexed ligand (Supporting Information, Figure S3). A complete analysis is encumbered by the very crowded spectrum.

Crystal Structure of *mer*-[Ru(QPzH)$_3$](PF$_6$)$_2$. Crystals suitable for X-ray diffraction were grown for the *mer*-**4**, and the resulting crystal structure with atom labels is shown in Figure 2 (left). Crystallographic data is shown in Table 1, and selected bond distances and angles are summarized in Tables 2 and 3, respectively; additional information is given in Supporting Information, Table S1. The three ligands are clearly nonequivalent, as was observed in the ^1H NMR spectrum, and hence they were given different labels, namely, a, b, or c. The differences between the three ligands are mainly due to distortions in the ligand backbone. The most obvious variation is the dihedral angle between the planes of the pyrazole and the quinoline heterocycles. For ligand a (Figure 2, left) the dihedral angle N2a−C10a−C9a−C5a is only 3.27°, and hence this ligand is nearly planar. For ligands b and c, the corresponding dihedral angles are 14.72° and 22.96°, respectively (absolute values). Hence, the ligand QPzH (**3**) is flexible enough to adopt several different modes, and in particular, to become planar, which is a notable difference compared to other quinoline-containing ligands (vide infra). Another distortion that is apparent in *mer*-**4** is the dihedral angles Ru−N1−C5−C9 (7.44−24.62°, absolute values) and Ru−N2−C10−C9 (3.60−4.92°), which measure how tilted the plane of the heterocycle is relative to the Ru−N bond of the same group. For ligand a in Figure 2 the tilt is small for both the pyrazole and quinoline groups. For ligands b and c, however, the quinolines are tilted to a greater extent (19.99 and 24.62°) than the pyrazoles (4.92 and 3.60°).

There are also some features that are similar among the ligands. All of the Ru−N_{Pz} coordination bond distances are of similar length, average 2.04 Å, and they are significantly shorter than the corresponding distances to the quinoline nitrogens, which, for all three ligands, are close to 2.12 Å. The bond angles around the metal cover the ranges of 86.20−95.28° for *cis* substituents and 176.58−177.68° for *trans* and are close to the ideal octahedral angles (90 and 180°, respectively). More specifically, the bite angles of the ligands (N1−Ru−N2) are all notably close (86.97−87.65°) to the ideal octahedral angle of *cis* substituents.

Furthermore, the crystal structure revealed one medium strong hydrogen bond (d = 2.78 Å, 156.7°) between the Pz amine group and the MeOH used as solvent (CH_3−O···H−N). However, this H-bond is not involved in any extended network and probably does not contribute much to the overall stabilization of the structure. For ligand a and b the distance between the pyrazole N−H hydrogen and the coordinating

Table 1. Crystallographic Data and Structure Refinement Details of *mer*-4

empirical formula	$C_{37}H_{30}F_{12}N_9OP_2Ru$[a]
formula weight (g/mol)	1007.7
temperature (K)	293
wavelength	0.710 73 Å
data collection	Oxford Diffraction Xcalibur Eos
crystal system	monoclinic
space group	$P2_1/n$
unit cell dimensions	a = 12.1633 (2) Å
	b = 16.1571 (2) Å
	c = 20.5034 (4) Å
	β = 100.7226 (15)°
volume (Å^3)	3959.05 (11)
Z	4
abs. coeff. (mm^{-1})	0.58
F(000)	2020
crystal size (mm^3)	0.18 × 0.13 × 0.12
2θ range for data collection (deg)	2.9−28.8
index ranges	h = ± 16
	k = ± 21
	l = ± 27
reflections collected	84 737
independent reflections	9809
R_{int}	0.073
GOF on F^2	1.99
$R[F^2 > 2\sigma(F^2)]$	0.061
$wR(F^2)$	0.132
largest diff. peak and hole (e Å^{-3})	2.13/ −1.20

[a]The formula represents the contents of the modeled unit cell and is lacking one hydrogen since the O−H hydrogen of the methanol molecule was not introduced into the model as described in the Experimental Section.

Table 2. Selected Bond Lengths and Ligand-Specific Angles for *mer*-4

	atom labels	ligand a	ligand b	ligand c
distances (Å)	Ru1 N1	2.117(4)	2.114(4)	2.125(4)
	Ru1 N2	2.052(4)	2.050(4)	2.031(3)
angles (deg)	N1 Ru1 N2	87.65(15)	87.55(14)	86.97(14)
dihedral angles (deg)[a]	N2 C10 C9 C5	3.27	−14.72	22.96
	Ru1 N1 C5 C9	−7.44	19.99	−24.62
	Ru1 N2 C10 C9	−3.72	−4.92	−3.60

[a]Measured using Mercury 3.1.

Table 3. Interligand Angles for *mer*-4

atom labels	angle (deg)
N1a Ru1 N1b	86.89(15)
N1a Ru1 N2b	94.85(15)
N1a Ru1 N1c	177.68(13)
N1a Ru1 N2c	95.28(14)
N2a Ru1 N1b	94.93(14)
N2a Ru1 N2b	176.58(16)
N2a Ru1 N1c	93.07(15)
N2a Ru1 N2c	86.20(14)

dx.doi.org/10.1021/ic502432c | Inorg. Chem. 2014, 53, 12778−12790

Table 4. Calculated Energy and Geometry Factors[a] for the *mer* and *fac* Isomers of $[Ru(QPzH)_3]^{2+}$

complex	quantity	exp[b]	GS	^{3}MLCT	^{3}MC
fac-$[Ru(QPzH)_3]^{2+}$	E (eV)		0.00	1.94	1.94
	R_{Pz}[c]		2.039 ± 0.004	2.05 ± 0.01	2.20 ± 0.18
	R_Q[c]		2.14 ± 0.02	2.11 ± 0.07	2.26 ± 0.21
	R_{tot}[c]		2.09 ± 0.06	2.08 ± 0.06	2.23 ± 0.18
	O[d]		3.73	3.74	6.83
	P[d]		20.07	22.46	30.86
mer-$[Ru(QPzH)_3]^{2+}$	E (eV)		0.00	1.96	1.89
	R_{Pz}[c]	2.04 ± 0.01	2.05 ± 0.01	2.05 ± 0.01	2.09 ± 0.05
	R_Q[c]	2.12 ± 0.01	2.13 ± 0.02	2.10 ± 0.08	2.39 ± 0.24
	R_{tot}[c]	2.08 ± 0.04	2.09 ± 0.05	2.08 ± 0.06	2.24 ± 0.23
	O[d]	3.36	3.41	3.57	8.03
	P[d]	13.46	17.41	23.25	63.93

[a]Distances in Å and angles in degrees. Deviations are calculated as σ_n values. [b]Calculated from crystal structure. [c]R is an average of metal coordination atom bond distances, where the error is the standard deviation. R_{Pz} and R_Q are the average Pz–Ru and Q–Ru bond distances, respectively. [d]Average deviation = Σ|ideal angle − measured angle|/n.

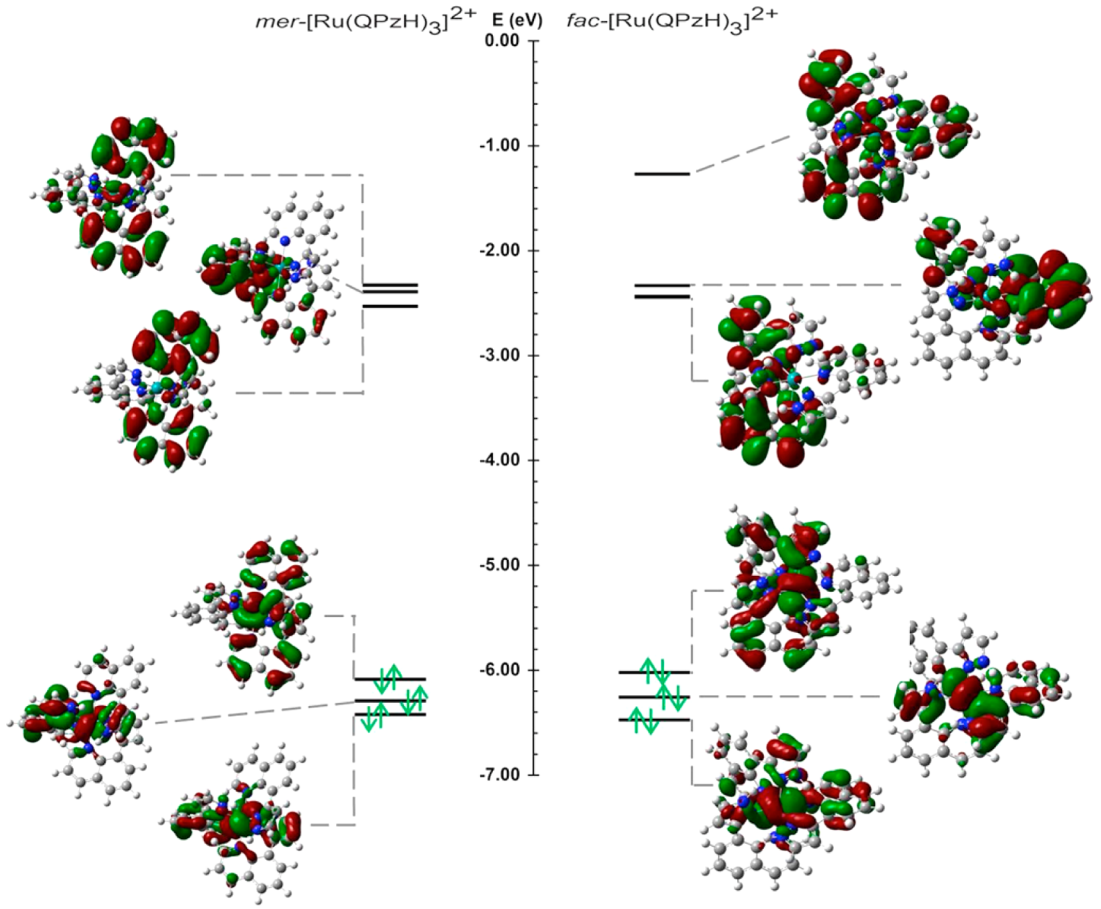

Figure 3. Calculated HOMO−2, HOMO−1, HOMO, LUMO, LUMO+1, and LUMO+2 molecular orbitals of the *mer* and *fac* isomers of $[Ru(QPzH)_3]^{2+}$.

nitrogen of the heterocycle toward which it is pointing is shorter (2.53 and 2.65 Å) than the sum of the van der Waals radii of H and N. Although this interaction is quite weak, similar ones have been claimed to be important for the acid–base chemistry of Ru-pyrazole complexes.[27,37]

Optimized Ground-State and First Triplet-State Geometries. Geometries of both *mer* and *fac* isomers were optimized using Gaussian09.[38] Complete geometry optimizations in the acetonitrile polarizable continuum model (PCM) were performed for the ground, ^{3}MLCT, and ^{3}MC states using the PBE0[39−41] functional, with the 6-31G(d,p)-SDD basis set combination, where the 6-31G(d,p) basis set was used for all atoms except Ru, for which SDD was employed. The optimized *mer* structure can be seen in Figure 2 (right), and the *fac* structure is available in Supporting Information (Figure S4).

The fully optimized excited-state local minima were identified and can be clearly distinguished on the basis of the significant change in spin density on the Ru atom as either MC- or MLCT-like (spin density characterization is available in Supporting Information, Figure S5). This is consistent with

dx.doi.org/10.1021/ic502432c | Inorg. Chem. 2014, 53, 12778−12790

expectations, since MC states formally have two unpaired electrons on the Ru metal center, while the MLCT states formally have one unpaired electron on the metal center and one on the ligands. The energies of the ground states of each isomer were set to zero for better discussion of their excited-state properties; however, the *mer* isomer ground state is slightly lower in energy, ~0.05 eV, indicating that it is somewhat more thermodynamically stable than the *fac* isomer. As expected from the crystal structure, the three ligands are not equivalent in the calculated *mer* isomer ground state; however, the respective bond lengths Ru−N_Q and Ru−N_{Pz}, are similar in all ligands. Both of the calculated isomers have shorter Ru−N_{Pz} bonds (R_{Pz}) and slightly longer Ru−N_Q bond lengths (R_Q), which agrees well with the crystal structure.

Geometric parameters like the *R*, *O*, and *P* parameters have proven useful for describing the geometric changes in the ground- and excited-state geometries for a range of metal complexes, including Ru[43,44] and Fe complexes.[45] The *O* parameter is a measure of the angular distortion from a perfect octahedron, given by the mean absolute deviation of the N−Ru−N angles from "ideal" octahedral values.[43] The average Ru−N bond distance and the deviation of the dihedral angles from perfectly planar (0°) have been included in Table 4 as the parameters *R* and *P*, respectively. Both the *mer* and *fac* isomers display octahedral geometry in the ground state and have imperceptible geometric changes from the calculated ground state to the ^{3}MLCT excited state. In contrast, the ^{3}MC geometries appear significantly distorted, with an ~0.2 Å elongation in the *mer* isomer average Ru−Q bond and a large angular distortion away from a perfect octahedron.

Perhaps the most striking feature though, is the large change in *P* value between ^{3}MLCT and ^{3}MC for the *mer* isomer, indicating that a large geometrical reorganization is needed to reach the ^{3}MC state. For the *fac* isomer this change is much smaller, indicating that there can be large differences in excited-state behavior even for complexes that are very similar in their ground states.

Electronic Structure and Absorption Spectra. The electronic structures of *mer* and *fac* isomers were also characterized through computational methods. While all three ligands in the *fac* isomer are degenerate, the *mer* isomer has, as noted above, nondegenerate ligands; since every Pz and Q has a different set of *cis* and *trans* substituents. For the *mer* isomer, the three highest occupied molecular orbitals (HOMO, HOMO−1, and HOMO−2) all show large density on the metal and can thus be assigned to the t_{2g} Ru orbitals, as is typically found for six-coordinated Ru-polypyridyl complexes.[8] The lowest unoccupied molecular orbitals (LUMOs) are instead mainly centered on the quinolinyl groups of the ligands, while the contributions from the metal and the pyrazolyl, respectively, are only very minor. The situation is nearly identical for the *fac* isomer. The first three calculated HOMOs and LUMOs can be found in Figure 3.

TD DFT was used to predict the electronic absorption spectra of the *mer* and *fac* isomers, respectively, Figure 4, and the vertical excitation energies and oscillator strengths are given in the Supporting Information (Table S2). The calculated spectra display the expected ^{1}MLCT band in the visible region, as well as the $\pi-\pi^*$ transitions in the UV region and an additional feature at ~300 nm, which was both MLCT and MC in nature. The experimental UV−vis spectrum of *mer*-**4** was recorded in acetonitrile (with excess triflic acid to ensure complete protonation), Figure 4. In the visible region, the

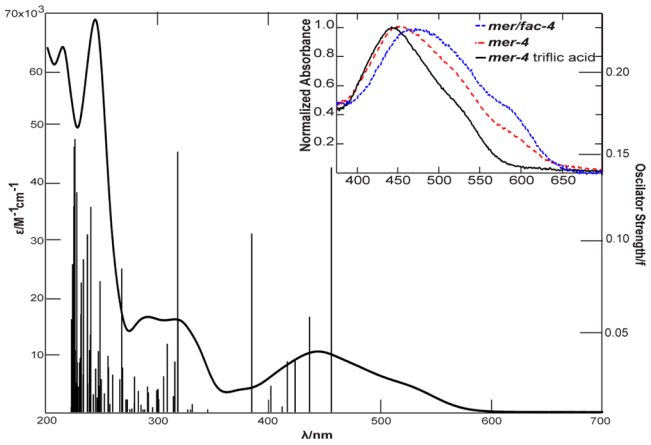

Figure 4. UV−vis spectrum for the fully protonated *mer*-**4** in acetonitrile with excess triflic acid with underlying calculated PBE0/6-31G(d,p)-SDD(acetonitrile) TD-DFT transitions. (inset) The difference between low-concentration *mer*-**4** in neat acetonitrile and in MeCN with excess triflic acid and the *mer*/*fac* **4** sample in neat acetonitrile. Computed UV−vis absorption spectra of for the *mer* and *fac* isomers are available in Supporting Information.

expected d$\pi-\pi^*$ ^{1}MLCT band is dominating the spectra[8] and displays significant absorption all the way out to 600 nm. The intense and broad feature observed between 280 and 370 nm is typical for Ru complexes incorporating the PzH motif.[27,28,46] Furthermore, the strong band in the UV region, centered at 245 nm, was attributed to ligand-centered $\pi-\pi^*$ bands in accordance with similar complexes.[8] This also corresponds well with the UV−vis spectrum of the free ligand only (λ_{max} = 243 nm). The TD-DFT predicts the experimentally obtained spectra both in shape and in absolute intensity. Computed UV−vis spectra, as well as all orbitals identified in the TD-DFT transitions, for both isomers, can be found in Supporting Information, Figures S6 and S7 and Table S2.

The inset in Figure 4 shows the absorption spectra, in neat acetonitrile, of the mixture of the *mer* and *fac* isomers, which exhibit a red shift of the maximum absorption compared to the pure *mer* sample. In addition, a more pronounced structure is observed in the MLCT band. The inset also shows a comparison between a dilute *mer* sample in acetonitrile and a sample of the same concentration, but with triflic acid added before measurement. The neat acetonitrile sample is somewhat red-shifted compared to the acidic sample. We attribute the broader visible absorption in the dilute *mer* sample to noncomplete protonation, as a red shift of the absorption is typically observed upon deprotonation of pyrazolyl groups.[27] Indeed, more concentrated samples display similar spectral shape as the acidic sample. To look at the spectral effects of deprotonation, measurements with added base (NaOH) were also performed and confirmed that deprotonation of the sample red shift the MLCT absorption significantly, which further supports this notion (Supporting Information, Figure S8). This behavior demonstrates that the NH-group of the pyrazole is indeed acting as a Brønsted acid, and consequently the compound is useful as a sensor for its environment. Although the acidic property of this complex is highly interesting, a detailed study of this behavior is beyond the scope of this study. The substantial red shift of the *mer*/*fac* mixture could possibly be due to higher acidity of the *fac* isomer. However, since the *fac* isomer is photosensitive, it is possible that this spectrum also shows contributions from degradation products.

dx.doi.org/10.1021/ic502432c | *Inorg. Chem.* 2014, 53, 12778−12790

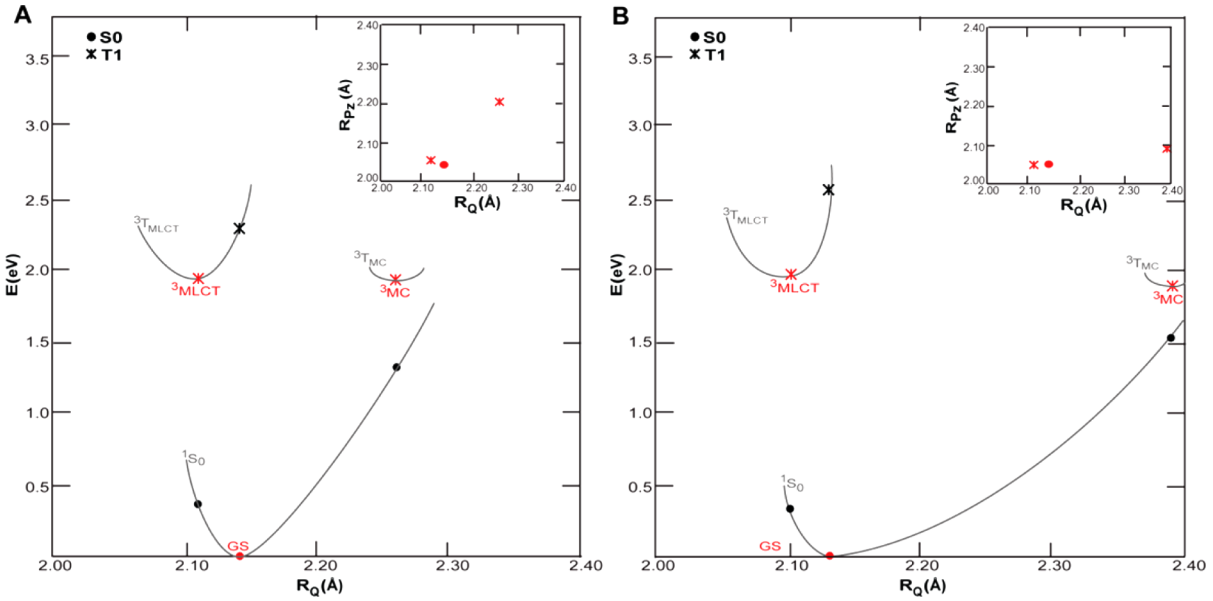

Figure 5. PPESs vs R_Q of the *fac* (A) and *mer* (B) isomers. Red points are optimized minima, and black points are single-point energies calculated at the minimum geometries. The gray potential energy curves connect states of the same spin type. (inset) The differences between calculated minima geometries in both R_Q and R_{Pz}.

Table 5. *R*, *O*, and *P* Parameters for a Number of Experimentally Determined Complex Structures, and Room-Temperature Excited-State Lifetimes if Reported[a]

	$[Ru(QPzH)_3]^{2+}$	$[Ru(bpy)_3]^{2+}$ [47]	$[Ru(QPy)(bpy)_2]^{2+}$ [17]	N3[50]	$[Ru(PyPzH)_3]^{2+}$ [36]	$[Ru(DQP)_2]^{2+}$ [19]
R^b	2.08 ± 0.04	2.06 ± 0.00004	2.07 ± 0.02	2.04 ± 0.03	2.06 ± 0.01	2.07 ± 0.04
$R_{Pz}{}^b$	2.04 ± 0.01				2.06 ± 0.007	
$R_{Py}{}^b$			2.08		2.06 ± 0.02	
$R_Q{}^b$	2.12 ± 0.01		2.11			2.09 ± 0.04
$O^{c,e}$	3.36	6.19	5.52	4.81	6.97	1.27
$P^{d,e}$	13.46	5.82	30.47[f]	5.74	1.28	37.5
τ,[g] ns		890[8]	~1[17]	30[51]		3000[18,19]

[a]Distances in Å and angles in degrees. All values are calculated from the complete set of bonds and angles given in the crystallographic information file (.cif). [b]*R* is an average of metal coordinating atom bond distances, where the error is the standard deviation. R_{Pz}, R_{Py}, and R_Q are the average Pz–Ru, Py–Ru, and Q–Ru bond distances, respectively. [c]*O* calculated from all the *cis*-N–Ru–N bonds (ideally 90°). [d]*P* calculated from all the ligand dihedral angles (ideally 0°). [e]Average deviation = Σ|ideal angle − measured angle|/*n*. [f]Dihedral angle of the biheteroaromatic ligand. [g]Room-temperature excited-state lifetimes measured in dearated solutions of either acetonitrile or methanol/ethanol.

Excited-State Properties. Visible light excitation of the *mer*-**4** and the *mer*/*fac*-**4** in deareated neat acetonitrile yielded no detectable signals in steady-state emission measurements. The same was true when excess triflic acid was added to ensure complete protonation of the pyrazole nitrogens. The lack of room-temperature emission indicates a fast nonradiative decay via the ^{3}MC state, supported by the nearly isoenergetic calculated ^{3}MLCT and ^{3}MC states. As seen in most photochemically active metal complexes, the ^{3}MLCT geometries are very similar to those of the GSs. However, the *mer* isomer has an ~0.3 Å elongation of the Ru–N_Q bonds in the ^{3}MC state, whereas the *fac* isomer only has an ~0.15 Å elongation of the Ru–N_Q bonds in its ^{3}MC state. In the *mer* isomer, triplet states preferentially place the unpaired electrons into the e_g* orbital that aligns with the *trans*-quinoline axis; however, the *fac* isomer bond elongation in the ^{3}MC state is accompanied by an additional elongation of ~0.2 Å of the Ru–N_{Pz} bonds since all quinoline groups are *trans* to a pyrazolyl.

To determine the potential energy surfaces related to the deactivation of the ^{3}MLCT state for both the *fac* and *mer* isomers, key structural parameters for MLCT to MC conversion pathways were identified from the relevant excited-state minimized geometries, notably the Ru–N_Q elongations as measured by R_Q. From each of the optimized minima, the corresponding singlet (S_0) and triplet (T) energies were calculated and plotted along the relevant coordinate as a projected potential energy surface (PPES)[45] (Figure 5). The insets in Figure 5 show the R_Q and R_{Pz} structural changes in each of the optimized structures. The *fac* isomer has less overall geometric change between the ^{3}MLCT and ^{3}MC minima supporting the notion of a more easily accessible ^{3}MC state. These PPESs give the first picture of relative states in the decay cascade, but a more detailed study would have to be performed to completely characterize the nature of the ^{3}MLCT-to-^{3}MC decay in either of the isomers. The calculated energies for the *mer* isomer suggest that the relaxed ^{3}MC state is 0.07 eV lower than the relaxed ^{3}MLCT state, indicating a main, nonradiative, decay pathway.

Electrochemistry. Cyclic voltammetry was used to investigate the redox properties of *mer*-**4** in dry acetonitrile with tetrabutylammonium hexafluorophosphate ($TBAPF_6$) as the supporting electrolyte. A reversible wave (as judged by peak

dx.doi.org/10.1021/ic502432c | *Inorg. Chem.* 2014, 53, 12778–12790

height and a peak splitting of ~60 mV) appeared at +0.57 V versus ferrocene ($Fc^{0/+}$) and was attributed to the metal-based $Ru^{III/II}$ oxidation process. Scanning to negative potentials gave rise to two irreversible features at −1.46 and −1.89 V versus $Fc^{0/+}$, respectively. On the basis of previous results these features were assigned to ligand-based reductions.[3,8]

DISCUSSION

The newly designed biheteroaromatic ligand QPzH (**3**) was synthesized and used to form a homoleptic, tris-bidentate ruthenium complex $[Ru(QPzH)_3](PF_6)_2$ (**4**) with six-membered chelate rings. In this section we discuss ground-state properties and evaluate the design criteria for the ground-state structure of $[Ru(QPzH)_3](PF_6)_2$ and compare with structurally related compounds. Furthermore, we discuss the excited-state equilibrium and the reason for the lack of room-temperature emission in $[Ru(QPzH)_3](PF_6)_2$.

Ground-State Properties. A detailed comparison between the calculated geometry and the obtained crystal structure confirms that the calculations match the experimental findings well. The good predictive power is further manifested in the agreement between calculated and experimental electronic absorption spectra. Several structural parameters deserve further discussion and comparison with relevant bi- and tridentate complexes incorporating either the Q or the Pz moieties. Table 5 reports the structural parameters *O*, *P*, and *R*, calculated from the crystal structure data that has been reported, for *mer*-**4** and a few other structurally related complexes that were included for comparison.

First of all, we note that for *mer*-**4**, the crystal structure revealed significant flexibility of the QPzH ligand upon coordination to ruthenium. In fact, the three ligands in the complex all have different conformations, explaining the clear separation of signals observed in ^{1}H NMR. In particular, one of the ligands is able to adopt a nearly planar mode with a dihedral angle between the planes of the two heterocyclic groups of less than 4°, which is close to the 2.2° that has been reported for $[Ru(bpy)_3]^{2+}$.[47] The two other ligands show modest dihedral distortion (15° and 23°) between the planes of the heterocycles. While the deviation from planarity is obvious (*P* values in Table 4 and 5), still the QPzH ligands are significantly less distorted than what has been observed in other complexes, for example, $[Ru(DQP)_2](PF_6)_2$,[18,19] $[Ru(bpy)_2(QPy)](PF_6)_2$[17] (Table 5), and $[Pd(QPy)(CH_3)](Cl)$[25] that all utilize the 8-quinolinyl-pyridine motif, and where dihedral distortions as large as 30−40° have been reported. This confirms our initial hypothesis that incorporation of a five-membered heterocycle provides a strategy to attenuate the distortions typically seen when the 8-quinolinyl motif is used in the ligand framework. It is especially noteworthy that despite the fact that $[Ru(QPzH)_3]^{2+}$ is a homoleptic complex, featuring three 8-quinolinyl motifs, all ligands are more planar than the one 8-quinolinyl ligand in $[Ru(bpy)_2(QPy)]^{2+}$.[17] If we instead consider the pyrazolyl group and compare $[Ru(QPzH)_3]^{2+}$ with $[Ru(PyPzH)_3]^{2+}$, where PyPzH is 2-{3-pyrazole}-pyridine, we see that the PyPz complex displays the lowest *P* value[48] of all listed in Table 5. This observation can be expected based on steric arguments, and it also further confirms our hypothesis that the incorporation of five-membered heterocycles will affect the dihedral distortions significantly, as is seen by comparing $[Ru(PyPzH)_3]^{2+}$ with $[Ru(bpy)_3]^{2+}$.

Table 4 reveals another interesting fact, namely, that the *P* factor is much larger in the ^{3}MC states than it is in the ground or ^{3}MLCT states. It has been previously observed, for the kind of complexes discussed here,[21,43,45] that the ^{3}MC state arises from populating the $d_{z^2}-e_g^*$ orbital on the metal center, significantly elongating one axis in the complex. This elongation leads to steric interactions that simply force one or more of the ligands to tilt when they are pushed away from the metal. We also note that the ^{3}MC *P* factor is twice as large in the *mer* isomer. While any explanation by necessity must be speculative, it is intriguing that the *mer* isomer is the more photostable one. Since it is able to accommodate the space needed for the large twist required on two of the ligands to maintain the short Ru−N_{Pz} bonds, while simultaneously elongating the N_Q-N_Q axis in the *mer*-^{3}MC state, it is somewhat surprising that this flexibility does not seem to cause permanent ligand loss.

Another design criterion in this work was that the ligand should facilitate an octahedral coordination, with bite angles close to 90 and 180° for *cis*- and *trans*-coordinating groups, respectively. A way to assess the overall octahedricity of a complex is through the *O* parameter (vide supra), and a systematic comparison of related complexes, as the one presented in Table 5, is informative. The comparison reveals that $[Ru(QPzH)_3]^{2+}$ is indeed close to octahedral with an *O* value of 3.36, which is much smaller than the 5.52 calculated from the crystal structure of $[Ru(bpy)_2(QPy)]^{2+}$, and $[Ru(bpy)_3]^{2+}$ is even less octahedral. Complexes like N3 (N3 is $[Ru(dcb)_2(SCN)_2]$, where dcb is 2,2′-bipyridyl-4,4′-dicarboxylate)[49] and $[Ru(PyPzH)_3]^{2+}$[46] both display large deviations from perfect octahedricity in their ground-state geometries. Interestingly, $[Ru(bpy)_3]^{2+}$ and $[Ru(PyPzH)_3]^{2+}$ are the two least octahedral complexes in this comparison. On the other hand, $[Ru(DQP)_2]^{2+}$ displays an almost perfect octahedral coordination sphere. This comparison clearly shows that ligands incorporating the 8-quinolinyl group typically result in complexes with coordination angles closer to ideal octahedral values. As mentioned previously, a close to perfect octahedral geometry is believed to influence the ^{3}MLCT-^{3}MC energy gap in such a way that excited state lifetimes are prolonged, due to less efficient nonradiative decay via the ^{3}MC state. However, considering the excited state lifetimes of the compounds in Table 5 (if reported) no such direct correlation seems to exist for the bidentate complexes discussed here.

Although the coordination sphere around the metal in *mer*-$[Ru(QPzH)_3]^{2+}$ displays angles very close to the ideal octahedral ones, there are significant geometrical deviations in the Ru−N bond distances. In *mer*-**4**, the distances from the metal to the nitrogens of the quinoline are all about 0.08−0.09 Å longer than those to the pyrazole nitrogens. The same trend, although somewhat less pronounced, was reported for $[Ru(bpy)_2(QPy)]^{2+}$, such that the Ru−N_Q bond is 2.11 Å, while the Ru−N_{Py} is 2.079 Å. This is closer to but still slightly longer than what has been reported for $[Ru(bpy)_3]^{2+}$ (2.06 Å). $[Ru(DQP)_2]^{2+}$ confirms this trend, with slightly longer Ru−N_Q (2.077 Å) and somewhat shorter Ru−N_{Py} (2.025 Å) bonds. In contrast, $[Ru(PyPzH)_3]^{2+}$ exhibits average bond lengths that are more or less the same for the pyridine and pyrazole motifs. Furthermore, we note that the overall N3 complex *R* value is somewhat shorter than that for the other complexes. In fact, the distance between the Pz unit and Ru in $[Ru(QPzH)_3]^{2+}$ is very similar to the average bond lengths in the N3 complex.

The trend in bond distances for *mer*-**4** is contrary to what would be expected, considering the basicity of the different ligand motifs, with pyrazoles typically being less basic (pyrazole conjugate acid pK_a 2.5)[52] than quinolines (quinoline conjugate

dx.doi.org/10.1021/ic502432c | Inorg. Chem. 2014, 53, 12778−12790

acid pK_a 4.9).[53] There are, however, studies that indicate that coordinated pyrazoles are stronger σ donors[54] but weaker π acceptors[27] than pyridyl groups, and thus, pyrazoles are likely stronger σ donors/weaker π acceptors than quinolines as well.[55] The stronger σ-donating ability of pyrazole could be the cause for the significantly shorter Ru−N_{Pz} bond length as compared to Ru−N_Q. We note that the Ru−N_{Pz} bond distance for ligand c, where the *trans* ligand is quinoline, is slightly shorter than the other two Ru−N_{Pz} bonds (2.03 Å vs 2.05 Å, Table 2), which may be the result of weaker σ donation of the quinoline. However, the stronger σ donation of pyrazole does not result in the Ru−N_Q bond *trans* to N2c becoming longer than the other two Ru−N_Q bonds. If we consider the complex *mer*-$[Ru(PyPzH)_3](PF_6)_2$, the crystal structure reveals Ru−N_{Pz} distances (2.048−2.061 Å) that are very similar to the Ru−N_{Py} distances (2.043−2.085 Å), and they show no correlation to the type of *trans* donor present.

If we instead examine the possibilities for steric interaction, it can be deduced from the crystal structure that the hydrogens on C1 on the quinoline groups (see Figure 2) are close to the atoms of the heterocyclic ring toward which they point—average distances to the three closest C or N atoms are 2.61, 2.63, and 2.65 Å. This should be compared to the hydrogen atoms on the N3 in the pyrazole group where the corresponding average distances are more than 0.3 Å longer, at 2.92, 3.03, and 3.04 Å, respectively. This indicates larger steric interactions for the quinolinyl group, which would result in longer Ru−N_Q coordination bonds. The planes of the quinoline groups are also significantly tilted, likely to reduce strain, whereas the pyrazole groups are not. Thus, the observed geometric differences can be attributed mainly to differences in steric requirements for the pyrazole and quinoline groups in $[Ru(QPzH)_3]^{2+}$, a finding that is consistent with what has previously been reported for the interactions between the QPy and bpy ligands in $[Ru(bpy)_2(QPy)]^{2+}$.[17] In fact, this steric effect is the reason why it is significantly easier to form metal complexes of the form $[M(ligand)_6]^{2+}$ with five-membered heterocyclic ligands, compared to pyridines or quinolines, which typically prefer to form $[M(ligand)_4X_2]$ complexes, where X is a small ligand, like a halide ion.[56] Only a few examples of stable $[M(Py)_6]$ complexes exist, including a hexapyridine Ru complex.[57,58] In that particular case, the coordination occurs at the expense of significantly elongated (2.10−2.14 Å) Ru−N_{Py} bond lengths (compared to Ru−N_{bpy} distances in $Ru(bpy)_3^{2+}$), which is likely due to a balance between σ interactions and steric hindrance.[57] For bidentate ligands like bpy and QPzH the planes of each pair of *trans* heterocyclic groups are, through geometric constraints, oriented orthogonal to each other, which minimizes competitive *trans*-π interactions. Furthermore, the steric interaction between ligands is reduced due to the small bite angle, but it becomes increasingly important when the bite angle of bidentate ligands increases as for QPzH. This argument can be extended to polydentate ligands as well. In summary, the difference in Ru−N_{Pz} and Ru−N_Q distances is likely due to differences in σ donor strength and, perhaps more significantly, in steric requirements of the Pz and Q groups. Steric effects, hence, need to be carefully considered when designing new ligands.[26]

The electrochemical experiments suggest that it is significantly easier to oxidize $[Ru(QPzH)_3]^{2+}$ compared to $[Ru(DQP)_2]^{2+}$ and $[Ru(bpy)_2(QPy)]^{2+}$; +0.57 V compared to +0.71 V[18] and +0.84 V[17] versus $Fc^{0/+}$, respectively, under similar experimental conditions. If we instead compare with the metal-based oxidation for $[Ru(PyPzH)_3]^{2+}$, which is reported to occur at 1.06 versus NHE,[46] which corresponds to ca. +0.6 V versus $Fc^{0/+}$, the two complexes behave very similarly. Thus, we attribute the lower oxidation potential in *mer*-**4** to the incorporation of the Pz motif into the ligand framework. Furthermore, the oxidation potential for $[Ru(QPzH)_3]^{2+}$ is very similar to that of the N3 complex,[49] despite the marked differences in electronic properties for the different sets of ligands in the two complexes. Irreversible ligand-based reductions for complexes incorporating the Pz unit have been previously reported. For example, a complex reported by Steel and Constable, with ligands where Py and Pz were connected through one of the Pz nitrogens (Py1Pz) also show irreversible reductions, at ca. −1.76 V versus saturated calomel electrode (SCE) for $[Ru(Py1Pz)_3]^{2+}$, which would then correspond to −2.16 versus $Fc^{0/+}$, thus suggesting it is significantly harder to reduce than is the QPzH complex reported here.[28] While the irreversible reductions make meaningful comparisons with, for example, $[Ru(DQP)_2]^{2+}$ and $[Ru(bpy)_2(QPy)]^{2+}$, hard to do, it is still worth noting that the QPzH ligand is easier to reduce than both the DQP and the QPy motifs when coordinated to Ru(II). These comparisons clearly show that the incorporation of the pyrazolyl group has profound effects on ground-state redox properties.

Excited-State Properties. As noted in the Results Section, $[Ru(QPzH)_3]^{2+}$ does not display any ^{3}MLCT emission under steady-state illumination at room temperature. This makes it similar to the $[Ru(bpy)_2(QPy)]^{2+}$ complex, which is also essentially nonemissive at ambient temperatures.[17] This is in sharp contrast to both $[Ru(DQP)_2]^{2+}$ and $[Ru(bpy)_3]^{2+}$, which are both strongly luminescent, with room-temperature excited-state lifetimes of 3 μs and ca. 1 μs, respectively.[8,19] Typically, Ru complexes that display no, or weak, emission at room temperature are believed to undergo fast deactivation of the emissive ^{3}MLCT state via the ^{3}MC state.[8,16] This deactivation pathway is governed by the energy barrier between the two states and also by the displacement of the ^{3}MC state relative to the ^{3}MLCT state. The energy difference can be affected, as mentioned in the introduction, by the coordination geometry around the metal center. Furthermore, as Hanan et al. have pointed out, increasing the σ donation ability can result in increased electron density on the metal, which will result in a stabilization of the MLCT states and a destabilization of the MC states.[59] If the excited-state energy becomes low enough, the energy gap law predicts that the nonradiative decay directly to the ground state will increase and thus lower both emission quantum yields and excited-state lifetimes.[60,61] Finally, it has been proposed that steric interactions can have a large impact on the excited-state properties.[17,32] Thus, there are many different factors that can influence the emission properties of a complex.

Clearly, the lack of emission in *mer*-$[Ru(QPzH)_3]^{2+}$ cannot be explained by poor coordination geometry. While it is not anywhere close to the almost perfect octahedron observed in $[Ru(DQP)_2]^{2+}$, it is significantly more octahedral than the highly emissive $[Ru(bpy)_3]^{2+}$. It seems, on the basis of the absorption spectrum and the calculated energies of the ^{3}MLCT and ^{3}MC states, unlikely that the excited-state energy would be stabilized to such a large extent that the energy gap law is the only governing factor for the lack of emission. One should also consider the fact that the ^{3}MC state is calculated to be the most stable state in the excited-state manifold for *mer*-**4**. While this

dx.doi.org/10.1021/ic502432c | Inorg. Chem. 2014, 53, 12778−12790

may at first seem like a viable explanation for the lack of emission, there are reports of other, strongly emitting Ru(II) complexes where similar calculations also suggest the ^{3}MC state to be the most stable state in the excited-state manifold, as it is for *mer*-**4**.[32]

Instead, we examine the bond lengths and the projected potential energy surfaces (Figure 5). Typically, shorter Ru−N bond lengths are expected to result in larger energy gaps between the ^{3}MLCT and ^{3}MC states. Inspection of the numbers in Table 5 reveals that the average Ru−N bond length in *mer*-$[Ru(QPzH)_3]^{2+}$ is the longest of all the complexes compared in this study. In addition to this general observation, we also note that, while the average bond length is just slightly longer, the Ru−N_Q bond distance is 2.12 Å, something that probably facilitates the ^{3}MLCT-to-^{3}MC crossing. The PPES for *mer*-**4** also suggest that a large geometrical distortion is necessary to reach the ^{3}MC state and that the nonradiative deactivation will be fast once the state has been populated, due to the small energy difference between the ^{3}MC potential curve and the corresponding ground-state potential curve. Thus, it seems likely that the lack of emission is at least partly attributable to steric distortions. However, we cannot exclude the different electronic properties of pyrazole compared to pyridine and quinoline ligands as part of the reason for the lack of emission in $[Ru(QPzH)_3]^{2+}$.

It is also interesting to contrast our computational results to the other complexes discussed here. In fact, a computational study of $[Ru(DQP)_2]^{2+}$ found that, applying the same level of theoretical sophistication, the ^{3}MC state is predicted to be lower than the ^{3}MLCT state, and still a 3 μs excited state lifetime is observed. That study also revealed the need to consider the multidimensional potential energy surfaces for all the different states involved in the deactivation of the ^{3}MLCT state to better explain some of the anomalies that have been observed in experiments. The electronic structure characterization furthermore suggests that the lowest LUMOs are almost entirely localized on the Q moiety. Here, we also note a difference compared to $[Ru(DQP)_2]^{2+}$ in which electronic structure calculations suggest an excited state more evenly distributed over the whole ligand framework.[18] These findings indicate that, as more systematic comparisons between experimental and computational results become available, a more complex picture of the factors governing ^{3}MLCT−^{3}MC equilibrium is emerging, and that no simple relationship between an isolated property, electronic or structural, and photophysical properties can be established. In this case, it seems probable that the long bond distances between Q and the metal is a large contributor to the short-lived ^{3}MLCT state.

Finally, we note that *mer*-**4** does not seem to be particularly sensitive to any permanent photoinduced ligand substitution. The *fac* isomer is indeed photosensitive, and separation and isolation of the *mer* isomer was possible by exposing the crude isomer mixture to light. This difference may reflect the calculated difference in ground-state energy, which indeed predicts the *mer* isomer to be thermodynamically stabilized compared to the *fac* isomer. While no detailed study of the photosensitivity of the *fac* isomer has been pursued here, it is clear that minor differences in structure of a complex can give very different reactivity and stability of a complex. Possibly, the elongation of the Ru−N_{Pz} bonds, as mentioned in the Results Section, may contribute to the lower photostability of the *fac* isomer. In contrast, the *mer* isomer is capable of dissipating the strain in the excited state by twisting its ligands, as indicated by the large *P* value in the ^{3}MC state. Previous studies of biheteroaromatic ligands rarely mention any light sensitivity of the Ru complexes, but two complexes containing pyrazole groups have been shown to photoisomerize[28] or dissociate a ligand[29] upon exposure to light. The fate of the *fac* isomer is unknown, but from the reaction yields in the synthesis and NMR data it can be concluded that it is not transforming into the *mer* isomer.

■ CONCLUSIONS

This study reports the first homoleptic Ru(II) complex using a bidentate biheteroaromatic ligand based on the 8-quinolinyl motif. A combination of experimental and theoretical techniques has been used to examine the structural, electronic, and photophysical properties of the new $[Ru(QPzH)_3]^{2+}$ complex based on the new QPzH ligand. The synthesis can either result in a statistical 3:1 *mer*/*fac* ratio of the complex, or, through controlled exposure to light, be tweaked to allow the isolation of the *mer* isomer only. Structure optimizations and X-ray crystallography both reveal three nonequivalent ligands, which are flexible enough to adopt several conformations, resulting in one ligand being close to planar, while the other two show large deviations from planarity. However, all the ligands show less strain than other quinoline-based bidentate ligands. Thus, the hypothesis that the combination of the quinoline-motif with a five-membered ring can reduce the steric effects and strain is confirmed.

The complex is essentially nonemissive at room temperature, and a closer examination of the observed behavior, in relation to structurally related complexes with very different photophysical properties, reveals that the excited-state properties critically rely on a combination of structural factors such as coordination geometry, bond distances, and steric interactions. This work also highlights the previously noted difference between bidentate and tridentate Ru complexes based on the same 8-quinoline ligand motif. The analysis presented here suggests that the longer Ru−N_Q distances are less important in tridentate complexes, while they, together with steric interactions between the ligands, have a large impact on the photophysical properties in bidentate complexes. Furthermore, photophysical and electrochemical measurements together with theoretical calculations suggest that the ground-state redox properties are, as expected, greatly affected by the incorporation of the Pz motif. Thus, we show that both structural and electronic properties, in the ground and individual excited states respectively, can be tuned by the combination of different heterocycles into the ligand framework. However, the resulting photophysical properties of such complexes are complicated and depend on the subtle balance of the ^{3}MLCT−^{3}MC equilibrium, which in turn depends on the electronic and steric interactions in the complex.

■ EXPERIMENTAL SECTION

All chemicals and solvents were purchased from Sigma-Aldrich and used as received unless noted otherwise. A literature procedure was used to prepare 8-acetyl-quinoline from 8-quinoline-carboxylic acid (Alfa Aesar).[35] The silica used for flash chromatography was 230−400 mesh and purchased from Sigma-Aldrich. The NMR spectra were recorded on a Varian Inova 500 MHz spectrometer, and the deuterated solvents were of at least 99.9% deuterated grade; all ^{1}H NMR resonances are referenced to the solvent residual signals. Light source used in the synthesis of *mer*-**4** was a cold light source from Leica, model CLS 150 XE. Light source for the NMR investigation was a 250 W tungsten lamp placed 0.6 m from the samples. Temperature

dx.doi.org/10.1021/ic502432c | Inorg. Chem. 2014, 53, 12778−12790

was controlled by fixing the samples on top of an ice−water bath, and the temperature never rose above 20 °C. When not exposed to light, samples were kept in the dark wrapped in metal foil.

Structural Determination. The dark red crystal was fixed to a glass fiber using Epoxy glue, and the single-crystal data were collected at room temperature on an Oxford Diffraction Xcalibur EOS CCD diffractometer with graphite monochromatised Mo Kα radiation (λ = 0.710 73 Å) operated at 50 kV and 40 mA, with a detector distance of 50 mm and θ_{max} = 28.8°. The Oxford CrysAlisPro RED software was used for data processing, including Empirical absorption correction using spherical harmonics, implemented in SCALE3 ABSPACK scaling algorithm.[62] Structural solution was accomplished using charge flipping as implemented in Superflip.[63] All refinements were performed using the JANA2006 software.[64] All non-hydrogen atoms were refined anisotropically, and all hydrogen atom positions were generated theoretically. The hydrogen atom on methanol (O−H) was not located and was chosen not to be generated theoretically. A summary of the crystallographic data and structure refinement details is given in Table 1. Further details on the crystal structure may be obtained in the Supporting Information.

Theoretical. The ground-state and triplet-state minima of the *mer* and *fac* isomers of $[Ru(QPzH)_3]^{2+}$ were investigated using DFT calculations. All quantum chemical calculations were performed using the Gaussian09 program.[38] The calculations comprise DFT calculations using the widely used PBE0[39−41] functional in conjunction with standard Gaussian-type orbital (GTO) basis sets of double-ζ quality, and the SDD Stuttgart/Dresden effective core potential (ECP) was used to provide an effective core potential for Ru[65] with a PCM solvent description for acetonitrile. Ground-state properties are calculated using the spin-restricted singlet formalism, while spin-unrestricted DFT (UDFT) calculations are performed for the lowest triplet-state calculations. All calculations were run with a total +2 charge on the complex, and no symmetry constraints were applied, allowing for possible Jahn−Teller effects. All minima were verified using vibrations calculated at the same level of theory following geometry optimizations, and the Mulliken spin density on the metal was used to indicate the nature of the excited states. TD-DFT calculations were performed at the same level of theory from the ground-state optimized structure to obtain the calculated absorption spectra.

Spectroscopy and Electrochemistry. UV−visible−near-IR (UV−vis−NIR) electronic absorption spectra were recorded with a Varian Cary 5000 UV−vis−NIR spectrophotometer (Varian, US), between 1600 and 200 nm. Steady-state emission experiments were carried out using an SPEX Fluorolog 3 spectrofluorimeter (Jobin-Yvon Spex) with either an R928 or R2658 photomultiplier tube (Hamamatsu, U.S.) as detector. Various excitation wavelengths in the visible region were obtained using a 450 W xenon lamp, and the emission spectra were recorded between 400 and 1000 nm.

Spectrophotometric grade acetonitrile (>99.5%, Sigma-Aldrich) was dried for a minimum of 24 h over 3 Å molecular sieves (Sigma-Aldrich) prior to use in emission and absorption spectroscopy. All optical spectroscopy measurements performed in acid had a triflic acid (Sigma-Aldrich) concentration of 1.2 mM, that is, minimum of 35 equiv of acid compared to complex, to ensure full protonation at all concentrations. Extinction coefficients were determined by linear regression over a series of 10 different dilutions of *mer*-**4**.

Cyclic voltammetry was performed in argon-purged solutions of *mer*-**4** (0.42 mM) in dry acetonitrile with 0.10 mM $TBAPF_6$ (Sigma-Aldrich) as supporting electrolyte with a scan rate of 0.1 V/s. Cyclic voltammograms were recorded on a CHI650A (CH Instruments Inc., U.S.) potentiostat in a conventional three-electrode configuration consisting of a platinum working electrode, a rod-shaped glassy carbon auxiliary electrode, and a salt-bridged (MeCN/0.1 M $TBAPF_6$) SCE reference electrode. Ferrocene was added after measurement as an internal standard, and the $Fc^{0/+}$ couple appeared at +430 mV with a 75 mV peak-to-peak separation.

Synthesis. *3-(Dimethylamino)-1-(8-quinoline)prop-2-en-1-one (**2**).* To a small round-bottom flask were added 601 mg (3.51 mmol) of 8-acetyl-quinoline (**1**), 46.8 mg (0.406 mmol) of L-proline, and 0.56 mL (4.22 mmol) of *N*,*N*-dimethylformamide dimethylacetal (DMF-DMA). After purging with dinitrogen the mixture was heated at 80 °C for 7 h, and then all volatiles were removed leaving a dark viscous oil. The crude product was purified by flash chromatography on silica, eluting first with ethyl acetate/heptane/triethyl amine (5:4:1, 200 mL in total) to remove impurities and then with ethyl acetate/triethyl amine (9:1, 500 mL in total) to elute the product. After evaporating the solvent, 741 mg (93%) of a brown viscous oil remained. ^{1}H NMR ($CDCl_3$, 500 MHz) δ 8.98 (dd, 1H, J = 1.5 Hz, J = 4.1 Hz) 8.15 (dd, 1H, J = 1.4 Hz, J = 8.3 Hz) 7.82 (dd, 1H, J = 0.9 Hz, J = 8.2 Hz) 7.77 (br. s, 1H) 7.54 (dd, 1H, J = 7.6 Hz, J = 7.6 Hz) 7.39 (dd, 1H, J = 4.1 Hz, J = 8.3 Hz) 5.67 (d, 1H, J = 12.9 Hz) 5.29 (s, 1H) 3.03 (s, 3H) 2.86 (s, 3H); electrospray ionization mass spectrometry (ESI-MS+) (CH_3CN): 227.118 [M + H$^+$]

*8-(3-Pyrazol)-quinoline (**3**). **Caution!** Hydrazine is a confirmed carcinogen, corrosive, toxic, and volatile. Hence, it should be handled with great care and only in well-ventilated fume hoods.*

To a solution of **2** (414 mg, 1.83 mmol) in absolute ethanol was added hydrazine monohydrate (88.8 μL, 1.83 mmol). The solution was heated at gentle reflux for 6 h and was then left to stir at room temperature overnight. A methanol/water mixture (1:1 by volume) was added dropwise until crystals started forming. When precipitation stopped, a 1.5 mL aliquot of the methanol/water mixture was added. The solution was left at room temperature to slowly concentrate for 2 h. Then the solid was filtered off, washed with 3 × 2 mL methanol/water (2:1), and dried under vacuum for 1 h to yield 170 mg of white crystals. Further concentration of the filtrate yielded more crystals, and in total 232 mg (65%) was collected. Elem. Anal. $C_{12}H_9N_3$: Observ. C, 73.9; H, 5.1; N, 20.4; Calc. C, 73.83; H, 4.65; N, 21.52%. ^{1}H NMR ($CDCl_3$, 500 MHz) δ 13.86 (br. s, 1H) 8.99 (d, 1H, J = 3.7 Hz) 8.24 (d, 1H, J = 8.0 Hz) 8.17 (d, 1H, J = 7.3 Hz) 7.78 (d, 1H, J = 8.0 Hz) 7.68 (s, 1H) 7.61 (t, 1H, J = 7.5 Hz) 7.50 (dd, 1H, J = 3.7 Hz, J = 7.9 Hz) 6.88 (s, 1H). UV−vis (CH_3CN): 243 nm (23 000 M^{-1} cm^{-1}); 323 nm (7000 M^{-1} cm^{-1})

*Tris-{8-(3-pyrazol)-quinoline} Ruthenium(II) Bis-(hexafluorophosphate), $[Ru(QPzH)_3](PF6)_2{\cdot}CH_3OH$, Mixture of mer and fac Isomers (mer/fac-**4**).* A suspension of **3** (53.0 mg, 0.272 mmol) and $Ru(DMSO)_4Cl_2$ (43.5 mg, 0.0898 mmol) in ethylene glycol was heated at 195 °C with stirring for 4 min during which the solution turned intensely dark red. After immediate cooling of the solution on a water bath to room temperature, 1.3 mL of methanol and 449 μL of a 1.0 M solution of $NaPF_6$ (0.449 mmol) in methanol were added, and a purple precipitate formed, which typically contained unidentified side products. Further precipitate formed when 3.5 μL of 65 wt % HPF_6 in water (0.028 mmol) was added, and the solid was filtered off and extracted with 2 × 0.2 mL of methanol/water (1:1) solution. Further 1.0 mL of methanol was added to the filtrate, and the solution was left in the dark for 36 h, upon which red crystals formed. Supernatant was decanted, and crystals were washed with methanol/water (1:1) solution and very quickly with cold methanol. The red crystals were dried under vacuum yielding 32 mg (37%). Product is a mixture of the *mer* and *fac* isomers in a ratio of 3:1 according to integration of ^{1}H NMR. The signals of the mixture can be assigned by comparison to the spectrum of the pure *mer* isomer and are presented separately below for the two isomers. The ratio appears to stay constant if samples, both liquid and solid, are kept in the dark. Elem. Anal. $C_{37}H_{31}F_{12}N_9OP_2Ru$, $[Ru(QPzH)_3](PF_6)_2{\cdot}CH_3OH$: Observ. C, 44.2; H, 3.4; N, 12.0; Calc. C, 44.06; H, 3.10; N, 12.50%; high-resolution mass spectrometry (HRMS) (ESI+, CH_3CN): m/z {rel. intensity} 343.57132 $[Ru(QPzH)_3]^{2+}$ {100} (calc. $C_{36}H_{27}N_9Ru^{2+}$ 343.57110), 491.055 27 $[Ru(QPzH)_2 - H]^+$ {9} (calc. $C_{24}H_{17}N_6Ru^{2+}$ 491.055 27), 686.135 52 $[Ru(QPzH)_3 - H]^+$ {32} (calc. $C_{36}H_{26}N_9Ru^+$ 686.13492). ^{1}H NMR (CD_3CN, 500 MHz) *Note: Integrals given are actual relative size of peaks in the spectrum.* δ 11.03 (br. s, 1H), 10.90 (s, 1H, *fac*), 10.82 (br. s, 1H), 10.74 (br. s, 1H), 8.76 (d, 2H, *mer*), 8.55 (dd, 1H, *mer*), 8.49 (dd, 1H, *mer*), 8.46 (dd, 1H, *mer*), 8.27 (dd, 1H, *mer*), 8.39 (dd, 1H, *fac*), 8.36 (dd, 1H, *fac*), 8.34 (dd, 1H, *fac*), 8.25 (dd, 1H, *mer*), 8.14 (dd, 1H, *mer*), 8.11 (d, 2H, *fac*, *mer*), 8.02 (t, 1H, *mer*), 8.00 (dd, 1H, *mer*), 7.86 (dd, 1H, *mer*), 7.81 (t, 1H, *fac*), 7.77 (m, 3H), 7.69 (m, 2H), 7.66 (dd, 1H, *fac*), 7.56 (t, 1H,

dx.doi.org/10.1021/ic502432c | Inorg. Chem. 2014, 53, 12778−12790

mer), 7.35 (m, 1H *mer*), 7.13 (m, 3H, *mer*), 7.05 (dd, 1H, *mer*), 7.01 (t, 1H, *fac*), 6.91 (m, 1H, *mer*), 6.94 (dd, 1H, *fac*)

Tris-{8-(3-pyrazol)-quinoline} Ruthenium(II) Bis-(hexafluorophosphate), [Ru(QPzH)$_3$](PF6)$_2$·CH$_3$OH, Pure mer Isomer (mer-4). A suspension of **3** (50.1 mg, 0.257 mmol) and Ru(DMSO)$_4$Cl$_2$ (40.8 mg, 0.0842 mmol) in ethylene glycol was heated at 195 °C with stirring for 4 min during which the solution turned intensely dark red. After immediate cooling on a water bath 1.0 mL of methanol was added along with 423 μL of aqueous 1.0 M $NaPF_6$ and 3.3 μL 65 wt % HPF_6 in water (0.026 mmol). Small amounts of a dark purple precipitate formed, which was removed by filtration and extracted with 3 × 0.2 mL water/methanol mixture (1:1), and this extract was added to the filtrate. A small amount of red crystals started forming in the filtrate, and these were removed by filtration, since they likely contained a mixture of *mer* and *fac* isomers, and they were extracted with 3 × 0.1 mL of methanol. The clear filtrate, with an intense red color, was treated with light from a Leica light source at intermediate power (4/6) for 6 h, and conversion of the *fac* to the *mer* isomer was monitored by withdrawing small samples, reducing the volume by evaporation, and precipitating the product completely by adding excess water. The precipitate was redissolved in CD_3CN and analyzed by NMR. When no *fac* isomer could be observed the volume of the reaction mixture was reduced on rotavap at 45 °C to ∼1 mL, and then water was added while agitating the solution until complete precipitation occurred. Product was recrystallized from a concentrated methanol solution yielding 19.7 mg (24%) of red crystals.

Elem. Anal. $C_{37}H_{31}F_{12}N_9OP_2Ru$, [Ru(QPzH)$_3$](PF$_6$)$_2$·CH$_3$OH Observ. C, 44.4; H, 3.2; N, 11.9; Calc. C, 44.06; H, 3.10; N, 12.50%; HRMS (ESI+, CH_3CN): *m*/*z* {rel. intensity} 343.571 59 $[Ru(QPzH)_3]^{2+}$ {100} (calc. $C_{36}H_{27}N_9Ru^{2+}$ 343.571 10), 491.055 34 $[Ru(QPzH)_2 - H]^+$ {3} (calc. $C_{24}H_{17}N_6Ru^{2+}$ 491.055 27), 686.13546 $[Ru(QPzH)_3 - H]^+$ {1} (calc. $C_{36}H_{26}N_9Ru^+$ 686.13492). ^{1}H NMR (CD_3CN, 500 MHz) 11.03 (br. s, 1H) 10.82 (br. s, 1H) 10.74 (br. s, 1H) 8.76 (d, 2H, *J* = 6.0 Hz) 8.55 (dd, 1H, J = 1.2 Hz, *J* = 5.3 Hz) 8.49 (dd, 1H, J = 1.1 Hz, *J* = 5.2 Hz) 8.46 (dd, 1H, *J* = 1.0 Hz, *J* = 8.1 Hz) 8.27 (dd, 1H, J = 0.9 Hz, *J* = 7.5 Hz) 8.25 (dd, 1H, *J* = 0.8 Hz, *J* = 8.1 Hz) 8.14 (dd, 1H, *J* = 0.9 Hz, *J* = 8.1 Hz) 8.10 (dd, 1H, *J* = 0.9 Hz, *J* = 8.2 Hz) 8.02 (t, 1H, *J* = 7.9 Hz) 8.00 (dd, 1H, *J* = 1.0 Hz, *J* = 7.4 Hz) 7.86 (dd, 1H, *J* = 0.8 Hz, *J* = 8.1 Hz) 7.77 (m, 3H) 7.69 (m, 2H) 7.56 (t, 1H, *J* = 7.8 Hz) 7.35 (m, 1H) 7.13 (m, 3H) 7.05 (dd, 1H, *J* = 5.5 Hz, *J* = 8.1 Hz) 6.91 (m, 1H)

■ ASSOCIATED CONTENT

Ⓢ Supporting Information

^{1}H NMR spectra, optimized GS geometries, Mulliken spin densities, tabulated bond distances and bond angles, UV−vis absorption spectra, tabulated results of DFT calculations, illustrations of HOMOs and LUMOs, and optimized coordinates for each stationary point geometry of select studied compounds. This material is available free of charge via the Internet at http://pubs.acs.org.

■ AUTHOR INFORMATION

Corresponding Author

*E-mail: abmaria@chalmers.se.

Notes

The authors declare no competing financial interest.

■ ACKNOWLEDGMENTS

The authors wish to thank Ångpanneföreningens forsknings-stiftelse (Åforsk) and the Swedish Research council (VR), the Craaford foundation, and the Knut and Alice Wallenberg (KAW) foundation for financial support. In addition, M.A. and J.H. thank the Area of Advance Nano at Chalmers for financial support. P.P. acknowledges support from the National Supercomputer Centre (NSC) and The Center for Scientific and Technical Computing at Lund University (LUNARC).

■ REFERENCES

(1) Alstrum-Acevedo, J. H.; Brennaman, M. K.; Meyer, T. J. *Inorg. Chem.* **2005**, *44*, 6802−6827.
(2) Gust, D.; Moore, T. A.; Moore, A. L. *Acc. Chem. Res* **2009**, *42*, 1890−1898.
(3) Sauvage, J. P.; Collin, J. P.; Chambron, J. C.; Guillerez, S.; Coudret, C.; Balzani, V.; Barigelletti, F.; Decola, L.; Flamigni, L. *Chem. Rev.* **1994**, *94*, 993−1019.
(4) Sun, L. C.; Hammarstrom, L.; Akermark, B.; Styring, S. *Chem. Soc. Rev.* **2001**, *30*, 36−49.
(5) Ardo, S.; Meyer, G. J. *Chem. Soc. Rev.* **2009**, *38*, 115−164.
(6) Barigelletti, F.; Flamigni, L. *Chem. Soc. Rev.* **2000**, *29*, 1−12.
(7) Friedman, A. E.; Chambron, J. C.; Sauvage, J. P.; Turro, N. J.; Barton, J. K. *J. Am. Chem. Soc.* **1990**, *112*, 4960−4962.
(8) Juris, A.; Balzani, V.; Barigelletti, F.; Campagna, S.; Belser, P.; Vonzelewsky, A. *Coord. Chem. Rev.* **1988**, *84*, 85−277.
(9) Abbotto, A.; Manfredi, N. *Dalton Trans.* **2011**, *40*, 12421−12438.
(10) Abrahamsson, M.; Hedberg, J. H. J.; Becker, H. C.; Staniszewski, A.; Pearson, W. H.; Heuer, W. B.; Meyer, G. J. *ChemPhysChem* **2014**, *15*, 1154−1163.
(11) Wang, Y. S.; Liu, S. X.; Pinto, M. R.; Dattelbaum, D. M.; Schoonover, J. R.; Schanze, K. S. *J. Phys. Chem. A* **2001**, *105*, 11118−11127.
(12) Elliott, C. M.; Hershenhart, E. J. *J. Am. Chem. Soc.* **1982**, *104*, 7519−7526.
(13) Lever, A. B. P. *Inorg. Chem.* **1990**, *29*, 1271−1285.
(14) Constable, E. C.; Steel, P. J. *Coord. Chem. Rev.* **1989**, *93*, 205−223.
(15) Calvert, J. M.; Caspar, J. V.; Binstead, R. A.; Westmoreland, T. D.; Meyer, T. J. *J. Am. Chem. Soc.* **1982**, *104*, 6620−6627.
(16) Hammarstrom, L.; Johansson, O. *Coord. Chem. Rev.* **2010**, *254*, 2546−2559.
(17) Abrahamsson, M.; Becker, H. C.; Hammarstrom, L.; Bonnefous, C.; Chamchoumis, C.; Thummel, R. P. *Inorg. Chem.* **2007**, *46*, 10354−10364.
(18) Abrahamsson, M.; Jager, M.; Kumar, R. J.; Osterman, T.; Persson, P.; Becker, H. C.; Johansson, O.; Hammarstrom, L. *J. Am. Chem. Soc.* **2008**, *130*, 15533−15542.
(19) Abrahamsson, M.; Jager, M.; Osterman, T.; Eriksson, L.; Persson, P.; Becker, H. C.; Johansson, O.; Hammarstrom, L. *J. Am. Chem. Soc.* **2006**, *128*, 12616−12617.
(20) Abrahamsson, M.; Wolpher, H.; Johansson, O.; Larsson, J.; Kritikos, M.; Eriksson, L.; Norrby, P. O.; Bergquist, J.; Sun, L. C.; Akermark, B.; Hammarstrom, L. *Inorg. Chem.* **2005**, *44*, 3215−3225.
(21) Parada, G. A.; Fredin, L. A.; Santoni, M. P.; Jager, M.; Lomoth, R.; Hammarstrom, L.; Johansson, O.; Persson, P.; Ott, S. *Inorg. Chem.* **2013**, *52*, 5128−5137.
(22) Schramm, F.; Meded, V.; Fliegl, H.; Fink, K.; Fuhr, O.; Qu, Z. R.; Klopper, W.; Finn, S.; Keyes, T. E.; Ruben, M. *Inorg. Chem.* **2009**, *48*, 5677−5684.
(23) Brown, D. G.; Sanguantrakun, N.; Schulze, B.; Schubert, U. S.; Berlinguette, C. P. *J. Am. Chem. Soc.* **2012**, *134*, 12354−12357.
(24) Jager, M.; Kumar, R. J.; Gorls, H.; Bergquist, J.; Johansson, O. *Inorg. Chem.* **2009**, *48*, 3228−3238.
(25) Delis, J. G. P.; Rep, M.; Rulke, R. E.; vanLeeuwen, P. W. N. M.; Vrieze, K.; Fraanje, J.; Goubitz, K. *Inorg. Chim. Acta* **1996**, *250*, 87−103.
(26) Mamo, A.; Aureliano, A.; Recca, A. *Molecules* **2010**, *15*, 1324−1339.
(27) Sullivan, B. P.; Salmon, D. J.; Meyer, T. J.; Peedin, J. *Inorg. Chem.* **1979**, *18*, 3369−3374.
(28) Steel, P. J.; Constable, E. C. *J. Chem. Soc., Dalton Trans.* **1990**, 1389−1396.
(29) Steel, P. J.; Lahousse, F.; Lerner, D.; Marzin, C. *Inorg. Chem.* **1983**, *22*, 1488−1493.
(30) Cramer, C. J.; Truhlar, D. G. *Phys. Chem. Chem. Phys.* **2009**, *11*, 10757−10816.
(31) Vlcek, A.; Zalis, S. *Coord. Chem. Rev.* **2007**, *251*, 258−287.

(32) Abrahamsson, M.; Lundqvist, M. J.; Wolpher, H.; Johansson, O.; Eriksson, L.; Bergquist, J.; Rasmussen, T.; Becker, H. C.; Hammarstrom, L.; Norrby, P. O.; Akemark, B.; Persson, P. *Inorg. Chem.* **2008**, *47*, 3540−3548.
(33) Borg, O. A.; Godinho, S. S. M. C.; Lundqvist, M. J.; Lunell, S.; Persson, P. *J. Phys. Chem. A* **2008**, *112*, 4470−4476.
(34) Fantacci, S.; De Angelis, F.; Selloni, A. *J. Am. Chem. Soc.* **2003**, *125*, 4381−4387.
(35) Taylor, R. *J. Chem. Soc. B* **1971**, 2382−2387.
(36) Metherell, A. J.; Cullen, W.; Stephenson, A.; Hunter, C. A.; Ward, M. D. *Dalton Trans.* **2014**, *43*, 71−84.
(37) Jude, H.; Rein, F. N.; Chen, W.; Scott, B. L.; Dattelbaum, D. M.; Rocha, R. C. *Eur. J. Inorg. Chem.* **2009**, 683−690.
(38) Frisch, M. J.; Trucks, G. W.; Schlegel, H. B.; Scuseria, G. E.; Robb, M. A.; Cheeseman, J. R.; Scalmani, G.; Barone, V.; Mennucci, B.; Petersson, G. A.; Nakatsuji, H.; Caricato, M.; Li, X.; Hratchian, H. P.; Izmaylov, A. F.; Bloino, J.; Zheng, G.; Sonnenberg, J. L.; Hada, M.; Ehara, M.; Toyota, K.; Fukuda, R.; Hasegawa, J.; Ishida, M.; Nakajima, T.; Honda, Y.; Kitao, O.; Nakai, H.; Vreven, T.; Montgomery, J. A., Jr.; Peralta, J. E.; Ogliaro, F. o.; Bearpark, M. J.; Heyd, J.; Brothers, E. N.; Kudin, K. N.; Staroverov, V. N.; Kobayashi, R.; Normand, J.; Raghavachari, K.; Rendell, A. P.; Burant, J. C.; Iyengar, S. S.; Tomasi, J.; Cossi, M.; Rega, N.; Millam, N. J.; Klene, M.; Knox, J. E.; Cross, J. B.; Bakken, V.; Adamo, C.; Jaramillo, J.; Gomperts, R.; Stratmann, R. E.; Yazyev, O.; Austin, A. J.; Cammi, R.; Pomelli, C.; Ochterski, J. W.; Martin, R. L.; Morokuma, K.; Zakrzewski, V. G.; Voth, G. A.; Salvador, P.; Dannenberg, J. J.; Dapprich, S.; Daniels, A. D.; Farkas, ñ. n.; Foresman, J. B.; Ortiz, J. V.; Cioslowski, J.; Fox, D. J. *Gaussian 09*, C.01.; Gaussian, Inc.: Wallingford, CT, 2009.
(39) Adamo, C.; Barone, V. *J. Chem. Phys.* **1999**, *110*, 6158−6170.
(40) Perdew, J. P.; Burke, K.; Ernzerhof, M. *Phys. Rev. Lett.* **1996**, *77*, 3865−3868.
(41) Perdew, J. P.; Burke, K.; Ernzerhof, M. *Phys. Rev. Lett.* **1997**, *78*, 1396−1396.
(42) Macrae, C. F.; Edgington, P. R.; McCabe, P.; Pidcock, E.; Shields, G. P.; Taylor, R.; Towler, M.; van De Streek, J. *J. Appl. Crystallogr.* **2006**, *39*, 453−457.
(43) Osterman, T.; Abrahamsson, M.; Becker, H. C.; Hammarstrom, L.; Persson, P. *J. Phys. Chem. A* **2012**, *116*, 1041−1050.
(44) Osterman, T.; Persson, P. *Chem. Phys.* **2012**, *407*, 76−82.
(45) Fredin, L. A.; Pápai, M.; Rozsályi, E.; Vankö, G.; Wärnmark, K.; Sundström, V.; Persson, P. *J. Phys. Chem. Lett.* **2014**, *5*, 2066−2071.
(46) Fung, A. K. M.; Chiu, B. K. W.; Lam, M. H. W. *Water Res.* **2003**, *37*, 1939−1947.
(47) Rillema, D. P.; Jones, D. S.; Woods, C.; Levy, H. A. *Inorg. Chem.* **1992**, *31*, 2935−2938.
(48) Lam, M. H. W.; Cheung, S. T. C.; Fung, K. M.; Wong, W. T. *Inorg. Chem.* **1997**, *36*, 4618−4619.
(49) Nazeeruddin, M. K.; Kay, A.; Rodicio, I.; Humphry-Baker, R.; Mueller, E.; Liska, P.; Vlachopoulos, N.; Graetzel, M. *J. Am. Chem. Soc.* **1993**, *115*, 6382−6390.
(50) Eskelinen, E.; Luukkanen, S.; Haukka, M.; Ahlgren, M.; Pakkanen, T. A. *J. Chem. Soc., Dalton Trans.* **2000**, *16*, 2745−2752.
(51) O'donnell, R. M.; Johansson, P. G.; Abrahamsson, M.; Meyer, G. J. *Inorg. Chem.* **2013**, *52*, 6839−6848.
(52) *The Chemistry of Heterocyclic Compounds;* Weissberger, A., Taylor, E. C., Eds.; Wiley: New York.
(53) Brown, H. C. *Determination of Organic Structures by Physical Methods;* Academic Press: New York, 1955.
(54) Canty, A. J.; Lee, C. V. *Organometallics* **1982**, *1*, 1063−1066.
(55) Gerloch, M.; Hanton, L. R. *Inorg. Chem.* **1980**, *19*, 1692−1698.
(56) Poddar, R. K.; Agarwala, U. *J. Inorg. Nucl. Chem.* **1973**, *35*, 3769−3779.
(57) Templeton, J. L. *J. Am. Chem. Soc.* **1979**, *101*, 4906−4917.
(58) Holah, D. G.; Fackler, J. P. *Inorg. Chem.* **1965**, *4*, 1112−1116.
(59) Medlycott, E. A.; Hanan, G. S. *Coord. Chem. Rev.* **2006**, *250*, 1763−1782.
(60) Caspar, J. V.; Kober, E. M.; Sullivan, B. P.; Meyer, T. J. *J. Am. Chem. Soc.* **1982**, *104*, 630−632.
(61) Kober, E. M.; Caspar, J. V.; Lumpkin, R. S.; Meyer, T. J. *J. Phys. Chem.* **1986**, *90*, 3722−3734.
(62) *SCALE3 ABSPACK—An Oxford Diffraction Program,* 1.171.35.21; Oxford Diffraction Ltd: Waltham, MA, 2005.
(63) Palatinus, L.; Chapuis, G. *J. Appl. Crystallogr.* **2007**, *40*, 786−790.
(64) Petricek, V.; Dusek, M.; Palatinus, L. *Jana2006—Structure Determination Software Programs,* Institute of Physics, Praha: Prague, Czech Republic, 2006.
(65) Dolg, M.; Wedig, U.; Stoll, H.; Preuss, H. *J. Chem. Phys.* **1987**, *86*, 866−872.